ASME Journal of Turbomachinery
Online journal at:
https://asmedigitalcollection.asme.org/turbomachinery

Aerothermal–Structural Optimization of a High-Pressure Turbine Rotor With Robustness Evaluation to in-Service Deterioration

Mario Carta[1]
Department of Mechanical Engineering,
University of Cagliari,
Cagliari 09123, Italy
e-mail: mario.carta@unica.it

Roberto Putzu
Department of Mechanical Engineering,
University of Cagliari,
Cagliari 09123, Italy
e-mail: roberto.putzu@unica.it

Tiziano Ghisu
Department of Mechanical Engineering,
University of Cagliari,
Cagliari 09123, Italy
e-mail: t.ghisu@unica.it

Shahrokh Shahpar
Fellow—Aerothermal Design
Fluid Mechanics,
Rolls-Royce plc,
Derby DE24 8BJ, UK
e-mail: shahrokh.shahpar@rolls-royce.com

This article presents a multidisciplinary optimization conducted on the high-pressure turbine rotor of a commercial turbofan engine. The rotor geometry is parametrized using a compact orthogonal design space, and the system's response is studied under the aerodynamic, thermal, and structural aspects via high-fidelity numerical simulations. The analysis is conducted using proprietary Rolls-Royce flow and structural solvers. The objective functions considered for the aerodynamic, thermal, and structural disciplines are, respectively, high-pressure stage isentropic efficiency, peak near-wall gas temperature, and peak von Mises stress on the rotor. The optimization is constrained by rotor capacity and high-pressure stage reaction degree. On the final three-dimensional Pareto front, two designs are selected, achieving a peak stress reduction of 17.5 MPa and a peak temperature reduction of 27.5 K, respectively. The sensitivity of these optimal designs to in-service degradation is then evaluated by applying various degrees of deterioration to the nominal designs. This deterioration is intended to replicate the erosion and deformation patterns observed on in-service blades after different numbers of operational cycles. The aerothermal performance of the optima is verified at a higher fidelity by conducting unsteady simulations.
[DOI: 10.1115/1.4069937]

Keywords: high-pressure turbine, multidisciplinary optimization, surrogate modeling, unsteady simulation, robustness evaluation, in-service deterioration, computational fluid dynamics (CFD), turbomachinery blading design

1 Introduction

During their operational life, high-pressure turbine (HPT) rotor blades experience extremely high temperatures, centrifugal, and gas loads [1,2]. In modern turbofan engines, turbine entry temperatures exceed 2000 K [3], thus requiring complex film-cooling systems to be put in place. Overheating of the rotor structure can promote erosion, which will locally cause geometric modification that can highly affect the blade's performance [4,5] and increase secondary flows, which enhance local heat transfer rates, accelerating the deterioration process even further [6]. The HPT rotor disk is often spinning at more than 10,000 revolutions per minute, which leads to high centrifugal stress on the blades. The rotor is also subject to high gas loads: an individual blade, about 60 millimeters tall, exchanges with the flow an amount of power comparable to that produced by a modern formula-1 race car [7]. In a three-shaft setup, the HPT rotor disk must generate enough power to drive multiple high-pressure compressor rotors. The HPT blade is thus a key component inside the jet engine, subjected to high temperatures and high mechanical stresses, and must operate with high aerodynamic efficiency to ensure the necessary amount of power generation. When it comes to modeling the behavior of this component, it is therefore of great importance to consider the multidisciplinary nature of the problem. This aspect must also be taken into account when it comes to optimizing this component, as it is often found that geometric modifications that improve the design from the aerodynamic point of view end up rendering it unfeasible under the structural and thermal aspects, and vice versa.

In the jet engine manufacturing world, automatic and multidisciplinary optimizations are still not routinely relied upon when it comes to turbomachinery blade design [8,9]. This is due to a number of challenges, which include the computational cost, the need for rapid and reliable mesh generation, and the complexity of modeling the interactions between different disciplines. Most of the studies that can be found in the literature are single-objective aerodynamic-oriented or two-objective at best. Additional objective functions and/or constraints are introduced on the structural or aeroacoustic side when dealing with fans and compressor blades or on

[1]Corresponding author.

Contributed by the International Gas Turbine Institute (IGTI) of ASME for publication in the Journal of Turbomachinery. Manuscript received June 27, 2025; final manuscript received September 13, 2025; published online December 2, 2025. Tech. Editor: David G. Bogard.

the thermal side (e.g., peak metal temperatures) for turbine optimization cases. Many solutions have been tested over the years to reduce computational cost, often by using "smart" optimization techniques and compact yet effective parametrizations. Toropov et al. [10] conducted an aerodynamic optimization on a compressor blade by using an FFD-based (Free Form Deformation) parametrization and an adjoint sensitivity analysis, followed by a multipoint approximation method (MAM) optimization. Cuciumita et al. [11] presented a structurally constrained adjoint-based aerodynamic optimization on a compressor testcase. Although the adjoint methodology often finds turbomachinery optimization applications, its stability becomes an issue when dealing with complex geometries. The MAM method was also used by Shahpar et al. [12] for a compressor case, using a set of design parameters from PADRAM (PArametric Design and RApid Meshing) [13] that create different shapes by re-cambering, leaning, and re-staggering the blade at various span sections. Seshadri et al. [14] conducted a robust design optimization of a compressor case using PADRAM's design space, by using the evolutionary multidisciplinary ARMOGA (Adaptive Range Multi-Objective Genetic Algorithm) algorithm [15] with the aim of desensitizing the geometry to tip clearance variations. Hu et al. [16] conducted an aerothermal optimization of a NASA C3X turbine blade with a proper orthogonal decomposition-based dimensionality reduction technique. The same test case was used by Song et al. [17] to perform an aerothermal optimization using conjugate heat transfer simulations. In both works just referenced, the authors highlighted the strong competition existing between aerodynamic and thermal performance objectives. Amaral et al. [18] presented a methodology that can be used to conduct aerothermal optimizations of HPT blades' internal cooling channels, minimizing coolant usage and maximizing the component's service life. The authors demonstrated this modeling technique on a parametrized HPT blade geometry, using conjugate heat transfer simulations and a lifetime model [19]. Many optimization studies relevant to this topic can be found in the literature; however, very few of them deal with real industrial geometries and boundary conditions, whereas the majority make use of publicly available testcases. These are often characterized by simple geometries, not representative of the ones used in industry or in commercial flight. To the authors' knowledge, no work has been previously published where a high-fidelity aerothermal–structural optimization is conducted on a real, industrial testcase. The present analysis is conducted by modeling the behavior of turbomachinery components belonging to a real modern commercial jet engine, using boundary conditions that are representative of the machine's actual operating points.

In this work, a metamodel-based aerothermo-structural optimization is carried out on a high-pressure turbine computational domain. The design space for the high-pressure rotor geometry consists of the inlet and exit metal angles, as well as the blade's camber, lean, and stagger at three span sections along the blade height. A constrained infill-based optimization [20] is conducted using the IRT (Technological Research Institute) Saint Exupéry's open-source optimization tool GEMSEO [21], starting from an initial design of experiments (DoE). Industrial-grade computational fluid dynamics (CFD) and structural finite element method (FEM) solvers are used to evaluate the performance of the different designs. After that, a radial basis function (RBF)-based supervised machine learning algorithm is used to build the metamodel upon the DoE training dataset, which is then searched using a multi-objective NSGA-II (Non-dominated Sorting Genetic Algorithm) optimizer. The initial DoE is updated with points taken from the Pareto front and verified through CFD and FEM analyses, and the process cycles until satisfactory convergence is reached. The objective functions considered for this study are high-pressure stage efficiency (η), peak adiabatic recovery temperature on the high-pressure rotor (HPR) surface (T), and peak von Mises stress (SVM) in the rotor structure. The optimization is constrained by capacity (reduced mass flow at the HPR exit) and reaction degree within a range of $\pm 0.1\%$ and $\pm 0.2\%$ of the baseline value, respectively. From the Pareto front, two optimal geometries are selected, and their thermal performance gains are verified by running unsteady (phase-lag) simulations. This frequency-domain-based technique was originally introduced by Erdos and Alzner [22] and He [23], and its usage can be found in many turbomachinery-related articles, where it demonstrates a good cost/accuracy balance for modeling unsteady rotor–stator interaction [24–27]. On the same optimum geometries, a robustness evaluation study is finally conducted, to assess their performance's sensitivity to real-world in-service deterioration. The deterioration metrics used in this last phase are obtained through a measurement campaign that was carried out on a large set of in-service blades.

The rest of the article is organized as follows: the modeling methodology, which includes a description of the CFD computational domain, design parametrization, boundary conditions, CFD and FEM meshing, and solving techniques, is described in the second section. The third section contains a description of the optimization methodology as well as the robustness evaluation techniques. The fourth section is dedicated to the presentation and discussion of the results of the optimization, unsteady verification, and robustness evaluation studies. The last section provides a summary of the findings of this work, with some concluding remarks.

2 Modeling Methodology

2.1 Geometry and Boundary Conditions. In the present study, numerical flow simulations are run on a one-and-a-half-stage computational domain, which includes the high-pressure stator (HPS), HPR, and intermediate-pressure stator (IPS). The assembly scheme corresponding to this multi-row domain is displayed in Fig. 1.

This domain exhibits two interfaces, marked in the figure as "A" between the HPS and HPR and "B" between HPR and IPS. When steady-state simulations are run, these interfaces are both mixing planes, while for unsteady simulations, a sliding plane is used at the interface "A" and a mixing plane in "B." For these unsteady runs, there is only interest in modeling the temperature migration through the high-pressure stage, hence why a mixing plane is used at the second interface. The main inlet boundary condition is imposed at the HPS inlet. This condition is defined as a subsonic bi-dimensional inlet field of total pressure, total temperature, flow angles, fuel mixture fraction, and turbulence-related quantities. The main exit of the assembled domain is defined as a bi-dimensional static pressure field at the IPS exit. This field was extracted from a previous multi-stage simulation executed on the baseline case, spanning the whole turbine. There are a number of secondary flow inlets and cavity slot inlets, as shown by the green arrows in Fig. 1, which are mainly used to provide the endwalls and shroud with some cooling as well as sealing the rotor disk at blade root height. Film cooling strip models of the Crawford-

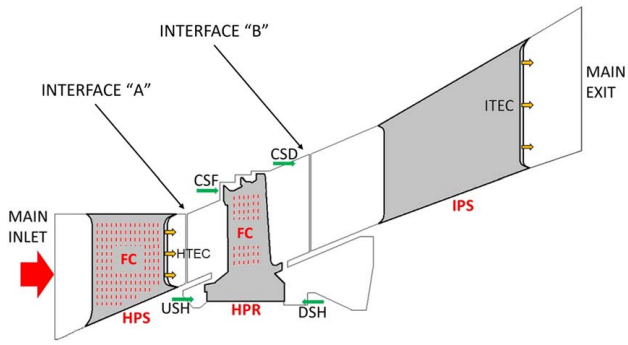

Fig. 1 Schematic of the multi-row computational domain for the aerothermal simulations. Film cooling (FC) strip models are indicated with dashed red lines. Acronyms can be found in nomenclature—Picture distorted and not to scale.

Table 1 Boundary conditions (see Fig. 1)

Patch	Type
HPS INLET	Subsonic inflow
HPS "FC," HPR "FC"	Film cooling source terms
HTEC, ITEC, USH, DSH, CSF, CSD	Prescribed mass flow inlets
INTERFACE "A"	Mixing plane (steady) Sliding plane (unsteady)
INTERFACE "B"	Mixing plane
MAIN EXIT	Static pressure outflow

type [28] are applied on the HPS and HPR blades and behave as source terms to simulate the presence of cooling hole rows, positioned in such a way as to replicate the real cooling hole arrangements on these components. These models are indicated with dashed red lines in Fig. 1. All simulations are run on single-passage domains, where each row contains a single blade and extends circumferentially by the corresponding pitch angle. Periodic boundary conditions are enforced on each row at the domain sides. The flow conditions being simulated in the present investigation are representative of the engine's "cruise" operating point. All of the boundary conditions discussed in this section are listed in Table 1.

For the structural (FEM) simulations, only the HPR geometry is considered. A fixed-constraint boundary condition is applied at the firtree of the blade. The rotational speed is provided to the structural solver to allow for the calculation of the centrifugal load. To apply the gas load boundary condition on the blade surface, the pressure field is imported for each case from the corresponding converged flow solution. The material's structural properties related to single-crystal titanium alloys are also provided to the FEM solver.

2.2 Design Parametrization. As stated in the introduction, the geometric part being parametrized in the present optimization is the HPR blade, while the two stator geometries are kept to the datum conditions. For these purposes, parameters from PADRAM's design space are used. These are representative of realistic transformations or deformations that are applied to the blade at a given span section. Figure 2 shows the four parameters that are used for the present optimization: DELT (circumferential lean), SKEW (re-staggering), LEMO (leading edge movement), and TEMO (trailing edge movement). The combination of the last two parameters provides a way of re-cambering the blade. Variation ranges for these design parameters are chosen to be as wide as possible without incurring negative mesh volumes, due to multi-block grid-generation failure. Three active control sections (S1, S2, and S3) are used, at span values, respectively, corresponding to 25%, 50% and 75%, leading to a total of 12 design variables. These are the same sections and parameters that were used in the uncertainty quantification study conducted in Ref. [4]. Two additional control sections are positioned at the hub and below the shroud (S0 and S4) and used to enforce locally null values for all the design parameters. This is done to ensure that the bottom and top sections of the blades are always consistent. This limitation in the parametrization is motivated by the practical need for being able to later merge the geometries with a standard root and shroud for structural meshing, as per the process described in Sec. 2.4. Deformations are interpolated using cubic splines in between the various control sections to ensure smooth transitions.

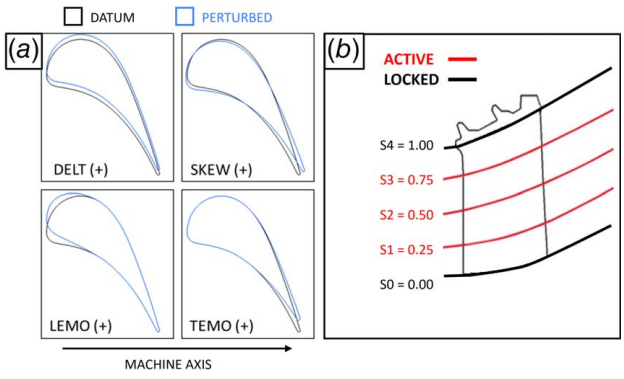

Fig. 2 Design parameters used on the HPR geometry at each control section (*a*). The baseline shape is shown in black, and the effect of applying each parameter to the section is shown in blue. (*b*) Active control sections are shown in red, and "locked" control sections, where parameters are set to zero, are shown in black.

2.3 Computational Fluid Dynamics Meshing and Solving Methods. This section describes the meshing and solving methodologies used for the aerothermal part of the optimization. Each row is meshed separately using PADRAM [13], which generates multi-block structured meshes with an H–O–H topology. On every wall of the computational domain, the grid's first cell height is set to achieve a $y+$ value lower than 1, which was verified during the mesh independence study. The results from this study are reported in Table 2, where the number of nodes was modified in the O-mesh along the three directions, namely the normal, tangential (side), and radial ones. The aerodynamic efficiency and peak HPR temperature values presented in Table 2 are expressed as deltas with respect to the value corresponding to case "H." The study led to the adoption of the settings corresponding to case "M." The meshes generated on the baseline geometries with said settings are displayed in Fig. 3 for the HPS (Fig. 3(*a*)) and HPR (Fig. 3(*b*)).

Table 2 Aerothermal mesh independence study

Case	Cells [10^6]	$\Delta\eta$ [%]	ΔTT_{max} [K]
L	6.7	−0.192	−5.5
M	11.2	−0.048	−1.4
H	20.3	–	–

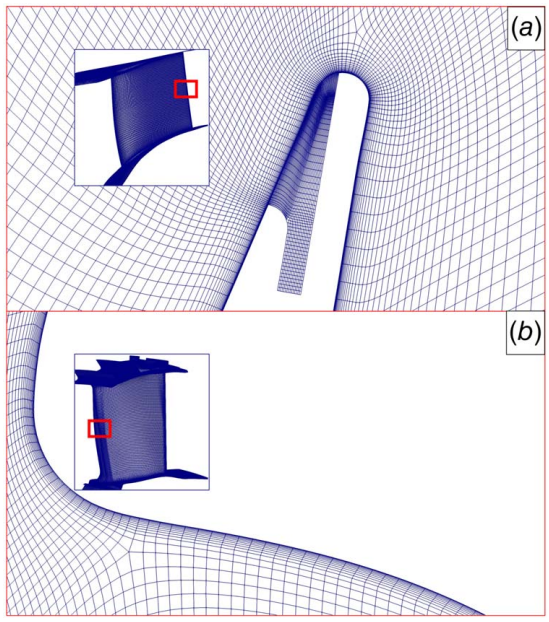

Fig. 3 PADRAM computational grids on the baseline geometries for the HPS (*a*) and HPR (*b*). The pictures show both full views of the surface meshes as well as blade-to-blade sections zooming in on the boundary layer mesh—Pictures distorted and not to scale.

A different meshing technique for the HPR row was used for the cases pertaining to the sensitivity analysis of shroud deterioration. These are the cases, which will be described later in Sec. 3.2 of this work, where the shroud part of the HPR blades is replaced with a deteriorated one from an in-service blade scan. For these "hybrid geometry" cases, the HPR grid is generated using Rolls-Royce's in-house version of Boxer [29].

Due to the level-set capability of Boxer, it can handle such hybrid geometries that are generated by merging different geometries. The HPR grids generated by Boxer with this technique are hexa-dominant. A number of 22 prismatic layers are generated on all of the walls of the HPR domain. First cell height is set to ensure a y^+ value equal to or below 1 on all the walls. Local refinement is used to enhance mesh density in critical areas such as the wake, cavities, and shroud. The optimal grid density setting used in the present work for the Boxer HPR meshes is inherited from a previous mesh independence study presented by the authors in Ref. [4].

Rolls-Royce's proprietary solver HYDRA [30] is used to perform the aerothermal flow simulations. Validation of this solver against experimental data in a high-pressure turbine case can be found in Ref. [31]. Three-dimensional Reynolds-averaged Navier–Stokes (RANS) simulations are performed in steady-state conditions, with k–ω shear stress transport [32] as a turbulence model. The iterative scheme is single-grid implicit with a CFL of 20. The convergence criterion for all the simulations is a residual value dropping under a threshold of 10^{-11} for all of the equations. Each CFD simulation required 5 h on 96 cores. As previously mentioned, the aerothermal quantities of interest being exported from the CFD solutions are the high-pressure stage isentropic efficiency (see Eq. (1)) and the peak adiabatic recovery temperature calculated on the HPR blade surface. In this case, adiabatic temperature is used as a figure of merit for the thermal side. Conjugate heat transfer simulations would provide a more accurate prediction but at a much higher cost. In previous works [33,34], the authors have found that lower peak adiabatic recovery temperatures will reflect in a same-sign variation of peak conjugate metal temperatures, albeit of a smaller amount. For this reason, the delta variations provided by this metric are used to guide the optimizer.

$$\eta = \frac{\sum_{i=\text{inlets}} (\dot{m}H_0)_i - (\dot{m}H_0)_{\text{exit}}}{\sum_{i=\text{inlets}} (\dot{m}H_0)_i - (\dot{m}H_{0\_\text{ideal}})_{\text{exit}}} \tag{1}$$

The efficiency metric was calculated by monitoring the flow at all of the inlets shown in the scheme of Fig. 1, as well as the HPR exit indicated as interface "B." The monitors provided values of mass flows and total enthalpy. These are calculated by mass-averaging the total pressures and temperatures at each inlet and exit considered for the calculation. In Eq. (1), $\dot{m}$ indicates a mass flow and H_0 stands for total enthalpy. The term with the subscript "ideal" in the denominator of Eq. (1) is calculated by isentropic expansion of each gas stream from its inlet conditions to the mass-averaged total pressure at the HPR exit, which is done automatically by the solver. The solver also calculated other efficiency metrics, including torque-based and polytropic. These different metrics all provided similar results. The isentropic-based metric was selected for consistency with previous work by the authors [4,6] on the same geometry.

Phase-lag simulations are used after the optimization to assess the optima's performance with a higher level of fidelity. The phase-lag technique uses a series of harmonic terms to express the periodically unsteady rotor-stator interaction. For further details on the implementation of this technique in a similar high-pressure turbine case, the reader can refer to Carta et al. [33,34]. To determine the number of harmonics, the study of Salvadori et al. [35] was taken as a reference. There, the authors had suggested that at least five terms should be used to properly describe the circumferential variability for a stator–rotor interaction of the kind modeled in the present study. In this case, six harmonics are used to describe the periodic variation through the sliding plane positioned at the interface "A" of Fig. 1. Each periodic cycle is divided into 396 time-steps, where 10 sub-iterations are performed. Ten phase-lag cycles are simulated, and the quantities corresponding to the last cycle are used for post-processing.

2.4 Finite Element Method Meshing and Solving Methods.

In order to calculate the stress field for the HPR blade corresponding to each design point during the optimization, a structural meshing and simulation system is put in place. For a given design point, the parametrized geometry definition of the HPR blade sections is imported from the aerothermal setup, and completed with the addition of a "root" made by a shank and a firtree. The latter is required to mechanically engage with the rotor disk slot. These parts are not present nor needed in the aerothermal setup, as they never interact with the flow. They are, however, needed in the structural setup to complete the component's geometry and enable the application of a fixed-constraint boundary condition for the FEM run. The same blade root geometry is hence imported from a CAD file and used for all of the design points. The shroud part is also imported from a CAD file, since this part of the geometry is not parametrized, and the CAD shroud definition is more detailed than its aerothermal counterpart. Figure 4 shows a representation of the baseline HPR mesh, where the constituent parts are differentiated by color and origin (aerothermal setup or CAD).

The hub is not parametrized, but is considered as a morphing part, and imported from the aerothermal setup together with the blade. This is due to the need of having a well-matched connection with the morphing blade. All of the different parts are imported into Boxer, where the structural domain meshing is performed. This is done by creating an internal octree mesh, followed by a body-fitting process using linear elements. On average, the resulting structural mesh has around 2.6 M elements. This grid density was chosen following a mesh independence study, whose results are reported in Table 3 for the quantity of interest SVM_{max} (peak von Mises stress). The stress values reported in Table 3 represent delta variations with respect to the finest case "H." The final mesh settings adopted are the ones indicated as "M" in Table 3.

The mesh is then imported into Rolls-Royce's in-house finite-elements package SC03 [36]. A validation study for this solver's thermo-mechanical capabilities for a high-pressure turbine case can be found in Ref. [37]. In SC03, the material properties and boundary conditions are applied. In reference to Fig. 4, the "blade" part is where the pressure load boundary condition is

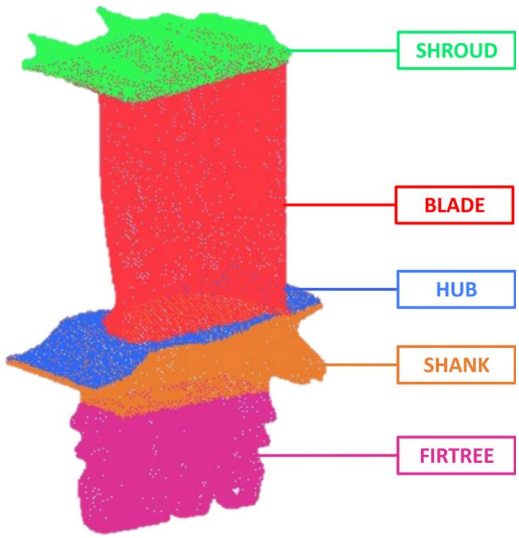

Fig. 4 HPR structural mesh with components in different colors. Dashed lines indicate a morphing component whose geometry was imported from the aerothermal setup. Remaining parts were imported from CAD files—Picture distorted.

Table 3 Structural mesh independence study

Case	Elements [$\cdot 10^6$]	ΔSVM_{max} [MPa]
L	1.2	−15.6
M	2.6	−3.2
H	4.4	–

Table 4 Optimization cycle convergence

Run	η error [%]	T error [%]	SVM error [%]	Converged
1	0.481	1.012	1.530	N
2	0.281	0.710	1.125	N
3	0.144	0.455	0.370	Y

applied, whereas the fixed-constraint boundary condition is applied to the "firtree" part. The solver employs a parallel sparse method. A FEM solution is sought by applying a loading ramp for the rotational speed. When forces and momentum equilibrium are reached, a results file is exported. From there, the von Mises stress field within the HPR structure is exported, and the peak value registered above the hub is saved. For the present work, values in the shank and firtree are not used to compute the stress objective function, as these areas were deemed to be less critical than the hub region, from a structural point of view.

3 Optimization Methodology

3.1 Multidisciplinary Optimization Setup. The optimization study presented in this article is metamodel-based. As indicated by the scheme of Fig. 5, the process begins with an initial DoE. For this purpose, the design space defined in Sec. 2.2 is populated using an initial Sobol [38] sequence of 200 points. The number of samples was chosen by multiplying the number of design parameters by 10 and adding ~50 more points for a thorough design space exploration [39]. The design parameter values corresponding to each point are given to PADRAM, which generates the modified HPR geometries and corresponding meshes. The multirow domain of Fig. 1 is subsequently assembled by adding the HPS and IPS meshes. On each of the DoE points, CFD and FEM simulations are launched in this order, and the three-objective function values are saved. Once the DoE is completed, the design data and objective function data are passed on to GEMSEO, which performs a RBF fitting. GEMSEO is then used to perform the three-objective optimization, which is constrained within ±0.1% baseline capacity and ±0.2% baseline reaction values.

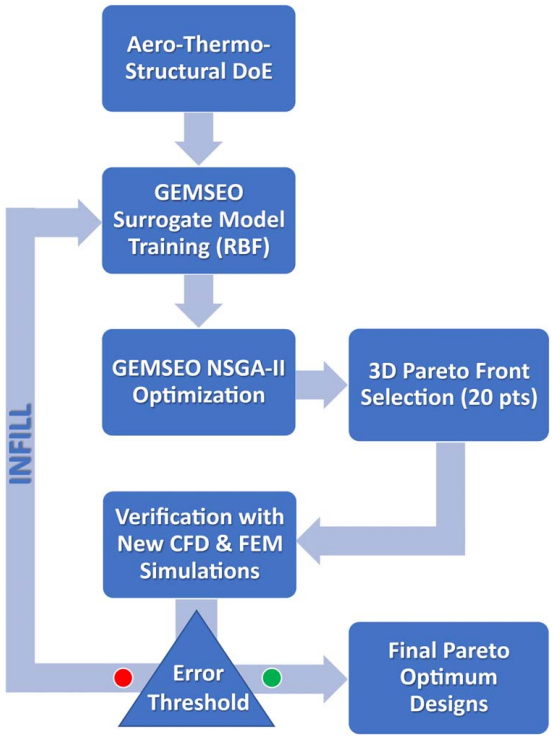

Fig. 5 Optimization cycle workflow. The stopping/convergence criterion is the bottom center block "Error Threshold," where the non-dominated metamodels' predictions are compared with CFD and FEM simulations, and an error metric is calculated.

The optimization is performed using the NSGA-II algorithm with a random seeding, a crossover probability of 0.9, and a mutation probability of 0.5. Population size is set to 100, with 100 generations for a total of 10,000 evaluations. This high number of evaluations was adopted because of the inexpensiveness of each surrogate run. Twenty points from the resulting Pareto front are selected by maximizing the sum of the relative distances and re-evaluated using CFD and FEM simulations. As shown in Fig. 5, this process is repeated until a satisfactory level of convergence is reached. Convergence is considered to be achieved when the norm of the objective functions' errors between metamodel prediction and CFD/FEM evaluations is lower than predefined thresholds of 0.2% for efficiency and 0.5% for maximum temperature and stress. Optimization convergence is reported in Table 4. At the end of the process, a total of 260 CFD and FEM evaluations have been performed. Optimum points are finally selected from the last verified Pareto set, among those that satisfy the capacity and reaction constraints. On the selected optimal geometries, higher fidelity phase-lag CFD simulations are conducted. This is mainly done to verify the thermal behavior of the designs: as highlighted in previous studies published by the authors, modeling the unsteady rotor–stator interaction can be highly impactful on HPR surface temperature prediction with differences exceeding 100 K in some cases [40,41]. Following this verification study, a robustness evaluation is conducted on the optimal designs. This process is described in the next section.

3.2 Sensitivity to In-Service Degradation. This section describes the methodologies used to evaluate the robustness of the optimal designs with respect to in-service deterioration. Previous studies have revealed the main deterioration modes experienced by these components during their operational life [4,6]. It was found that the aerodynamic performance of the baseline design is primarily sensitive to shroud deterioration, and secondarily to airfoil deformations taking place just below the shroud.

For the present study, two kinds of sensitivity analyses are performed. First, the effect of shroud deterioration on the baseline and optima's performance levels is assessed. Second, the effect of deformation of the blade sections is studied. The data for both shroud and blade deterioration were obtained by the authors in previous work [4] through a reverse-engineering procedure carried out on a set of 120 in-service blades. This ensures that the data collected reflect realistic deterioration modes, enabling a meaningful evaluation of the sensitivity to the baseline and optimal designs to the real deformations encountered during the blades' life.

In terms of robustness assessment with respect to shroud deterioration, as shown in Fig. 6(*a*), five shroud combinations are tested, with increasingly high levels of deterioration. In the figure, shroud deterioration is expressed as a percentual value ranging from 0 (design intent shroud) to 1 (heavy erosion, deformation and wear, and worst case of the set). The original shroud part of the baseline and optima is cut off and replaced with a deteriorated specimen. A new fluid domain mesh is then generated for each "hybrid" HPR geometry using Boxer. The multirow assembly (see Fig. 1) is then generated with the same process described in

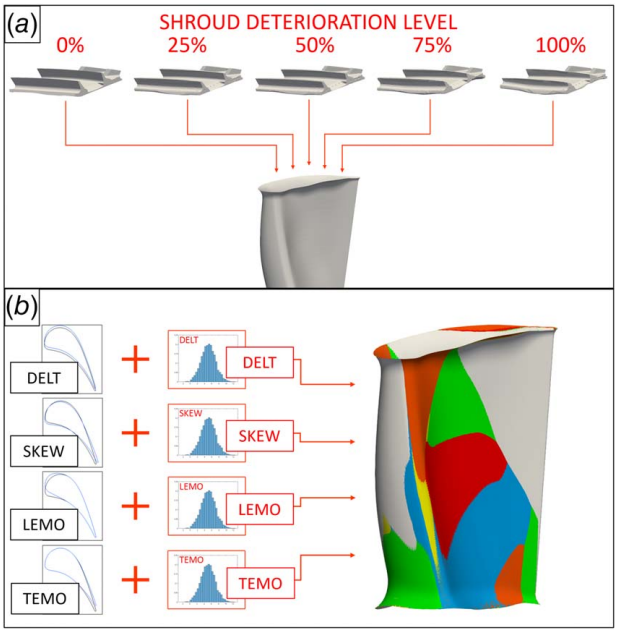

Fig. 6 Modifications applied to the optimal designs to assess the designs' robustness to in-service deterioration in terms of shroud deterioration (*a*) and blade design perturbation (*b*)—Pictures distorted

Sec. 2.3, and each "hybrid" case is then simulated through steady-state CFD. For the purpose of assessing the designs' robustness to blade airfoil deformation, as indicated in Fig. 6(*b*), variants of the baseline and optimum cases are tested by applying perturbations to the design parameters. These are the same parameters discussed in Sec. 2.2. As discussed, the perturbations have been obtained via a reverse-engineering/uncertainty quantification campaign. Figure 7 shows the frequency distributions for some of the design parameters (LEMO and TEMO) at the three control sections. Starting from each geometry considered for the robustness evaluation study (baseline and selected MDO (Multi Disciplinary Optimization) optima), a new set of variants is obtained by applying different perturbation combinations, and the perturbed HPR geometries are meshed. Both of these steps are done in PADRAM. For each case, the multi-row domain is then assembled, and a steady-state CFD simulation is launched.

4 Results and Discussion

4.1 AeroThermal–Structural Characterization. This section is dedicated to describing the main flow and structural phenomena that characterize this component's baseline behavior. This is done to gain an initial understanding of the main mechanisms responsible for aerodynamic losses, peak temperatures, and peak stresses on this design.

As for any gas turbine high-pressure section, the aerodynamic loss mechanisms are fundamentally tied to a few factors, namely (I) profile losses, (II) profile incidence losses, (II) secondary flow losses, (III) blade tip clearance losses, (V) coolant injection aerodynamic losses, and (VI) coolant injection thermodynamic losses [42–44]. As shown in Prof. Denton's work [45], term (III) referring to tip clearance losses is a highly important one. For the specific blade design studied in the present work, this effect was previously confirmed in studies carried out by the authors in Refs. [4,6]. Detailed investigations performed on in-service specimens of the blade have shown that an increase in tip leakage flow, be it through the shroud gap or the tip gap, accounts for around 80% of the total stage efficiency loss. In the same study, it was also found that this design's aerodynamic performance is highly sensitive to profile deformations capable of inducing a throat area variation. Among these, the most prominent is found to be a trailing edge (TE) re-cambering (opening up) below the tip. This design is found, within a certain range, to be less sensitive to a variation of the inlet metal angle,

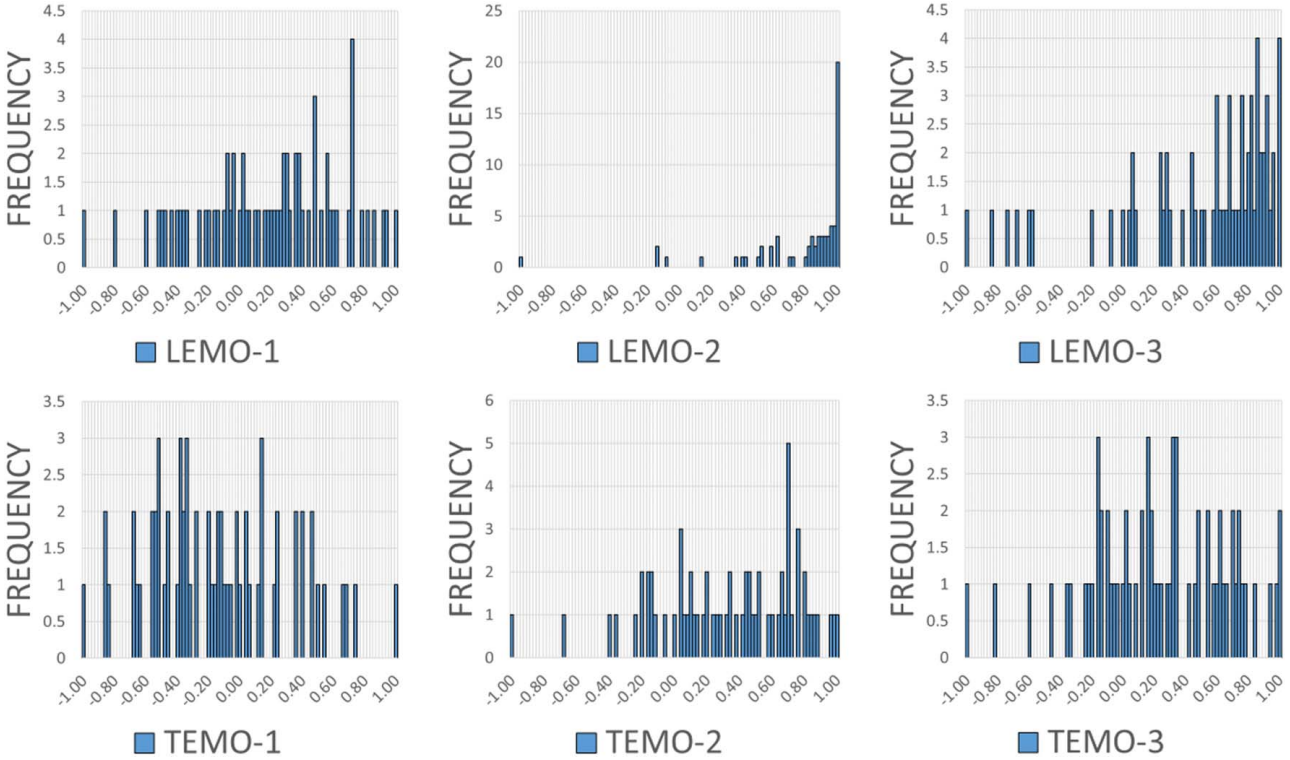

Fig. 7 Frequency distributions for some of the parameters (LEMO and TEMO) obtained through uncertainty quantification on the design parameters of Sec. 2.2—suffixes −1, −2, and −3, respectively, indicate section S1, S2, or S3 (see Fig. 2)

and this was attributed to the relatively large leading edge (LE) radius.

Peak adiabatic recovery temperatures, for the rotor design and boundary conditions under study, are reached at the midspan section in the LE region, close to the stagnation point, despite this area hosting a relatively high number of cooling hole rows. The span coordinate of this high-temperature area is mostly determined by the radial inlet temperature distribution delivered by the combustor. A considerable temperature difference is observed between the rotor's pressure and suction side surfaces, which can be traced back to the Kerrebrock–Mikolajczac effect, also known as "hot streak segregation" [46]. A can-type combustor will commonly produce a series of high-temperature streaks that migrate through the high-pressure turbine. Due to their higher streamwise velocity and cross-flow vorticity, combustor hot streaks approach the rotor with an incidence angle that is larger than that of the surrounding flow. This causes them to predominantly impinge on the pressure surface of the blade, rather than the suction surface. Steady-state and phase-lag RANS simulations both predict the same location for the peak temperature area on the rotor surface, albeit the latter predicts significantly higher peak values (~100 K), which is in line with previous findings [33].

For structural stress modeling, the blade is being subjected to centrifugal and gas pressure loads. The thermal load is not being considered for the purposes of this work. Two high-stress regions are located in the blade's structure. The first of these is in the firtree area (see Fig. 4). In particular, high levels of compression and shear are found in the lateral pressure faces where contact stress is developed [47]. A horizontal traction band can be observed in the shank area (see Fig. 4). The second key region is the suction side fillet area at the blade hub, where considerable bending moment is exerted, due to the centrifugal force attempting to "straighten" the blade. It is found that approximately 75% of the von Mises stress in both the firtree and fillet areas is due to the centrifugal force, with gas loads accounting for the remaining 25%.

4.2 MultiDisciplinary Optimization Results. The three-dimensional Pareto front produced by the optimization process at the last iteration (see Table 4) is displayed in Fig. 8 using bi-dimensional plots combining two-objective functions at a time. It is interesting to note the linearity that characterizes the stress versus the temperature front on the top of Fig. 8. Quadratic behavior can be observed on the other two fronts. Two points are selected from the final non-dominated set, namely the best-performing ones, respectively, in terms of efficiency and temperature, with stress levels equal to or lower than the baseline one.

The metamodel is found to have slightly overpredicted the aerothermal performance gains for these points. The CFD- and FEM-verified performance values of these designs correspond to the "OPT #1" and "OPT #2" points in the plots of Fig. 8. The plots also include the points corresponding to the baseline design's performance. The OPT#1 design is associated with an increase in HPT stage aerodynamic efficiency (+0.16%) and a 17.5 MPa reduction in peak HPR stress. This is accompanied by a limited reduction in peak temperature (−5 K). On the contrary, OPT #2 achieves a significantly lower peak HPR surface temperature (−27.5 K), albeit associated with a stage efficiency loss of 0.28% and relatively negligible improvements in terms of stress reduction (−3 MPa). Figure 9 shows frontal views of the optimal designs selected from the Pareto front of Fig. 8, as well as the datum geometry for reference.

It can be seen that both optima display modifications at both the LEs and TEs. These are highlighted in the lower half of the figure, where sections of the three blades for various span values are displayed. In the spanwise direction, both optima appear to display the same "curvy" TE profile, which is governed by the "TEMO" design parameter (see Fig. 2). In particular, the effects of negative TEMO can be seen on the upper half of both optima's span. It is worth noting that, even if these two designs (OPT #1 and OPT

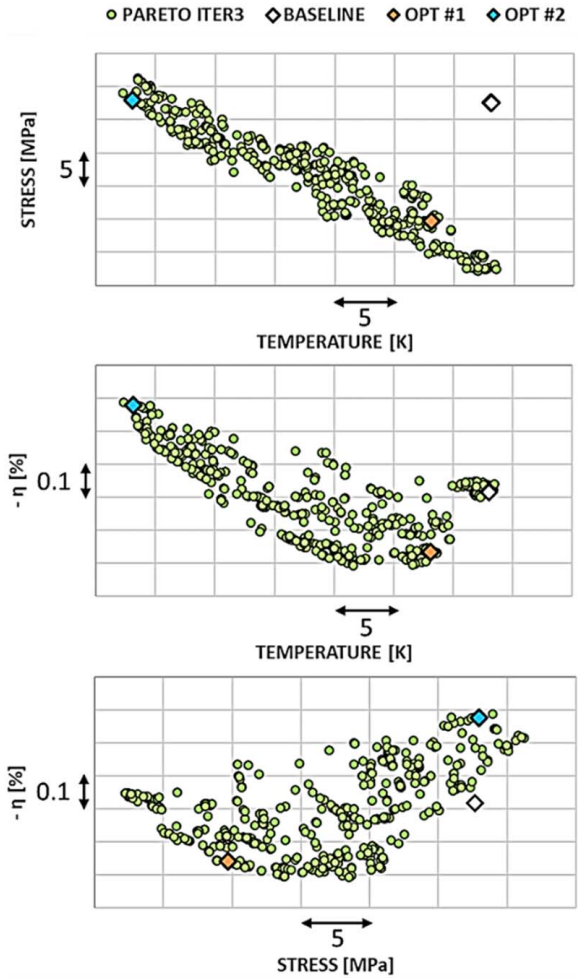

Fig. 8 Final metamodel-predicted Pareto fronts of the multidisciplinary optimization. The three-dimensional Pareto front is represented in bi-dimensional plots combining two-objective functions at a time. Points corresponding to the baseline and two selected optima after CFD and FEM verification are included.

#2) are found on opposite ends of the objective functions' space, the optimizer is pursuing the same TE profile on both. The same pattern was found on a large majority of feasible optima from the Pareto front of Fig. 8. It appears as if the optimization had converged to this deformation pattern as the best way of obtaining high performance levels while maintaining constraint compliance. Figure 10(*b*) shows a plot of spanwise isentropic efficiency delta (with respect to the baseline) calculated from the RANS solutions of the HPR rows. This efficiency metric is calculated for each case by circumferentially averaging temperatures and pressures at sections 0.25 chords upstream of the LEs and 0.25 chords downstream of the TEs. The formulation of Eq. (1) is then used to compute isentropic efficiency for each "constant-span streamline," accounting also for coolant injections from the Crawford-type sources. This calculation is based on the hypothesis of negligible spanwise migration of the flow streams as they travel through the blade passage. These streamlines are represented schematically in Fig. 10(*a*), covering the whole span of the blade from the hub to just below the shroud. As discussed in Sec. 4.1, this design's aerodynamic performance is known to be remarkably sensitive to modifications in the TE camber. In conjunction with the section views shown in Fig. 9, the curves in Fig. 10(*b*) show the beneficial effects of the high-span TE modifications in terms of isentropic efficiency.

Figure 11 shows the effects of different geometric modifications on the local flow-fields. This information can be used to explain

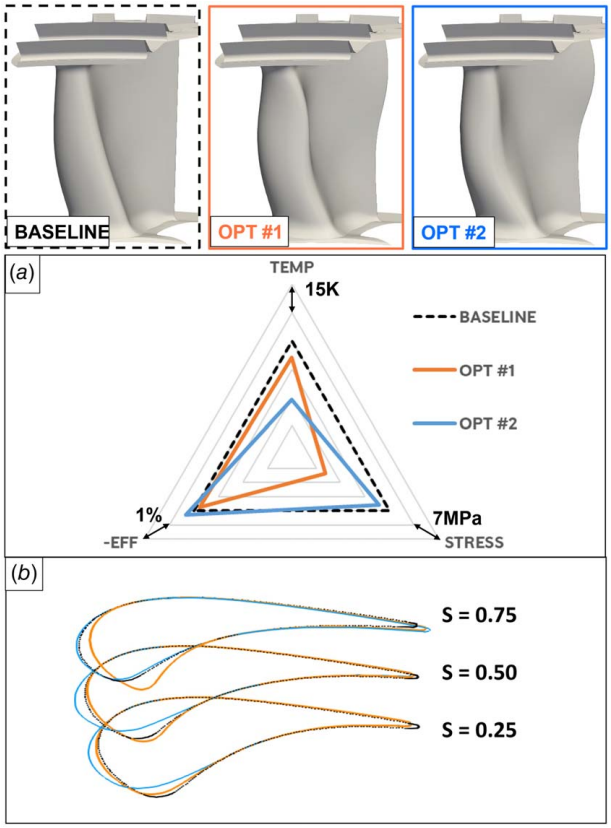

Fig. 9 Frontal views of the baseline and optimal HPR geometries following the same nomenclature of Fig. 8. Objective function values are displayed in the triangular plot (*a*). Constant-span sections are shown in (*b*) with the same coloring scheme. Pictures representing the geometries are distorted.

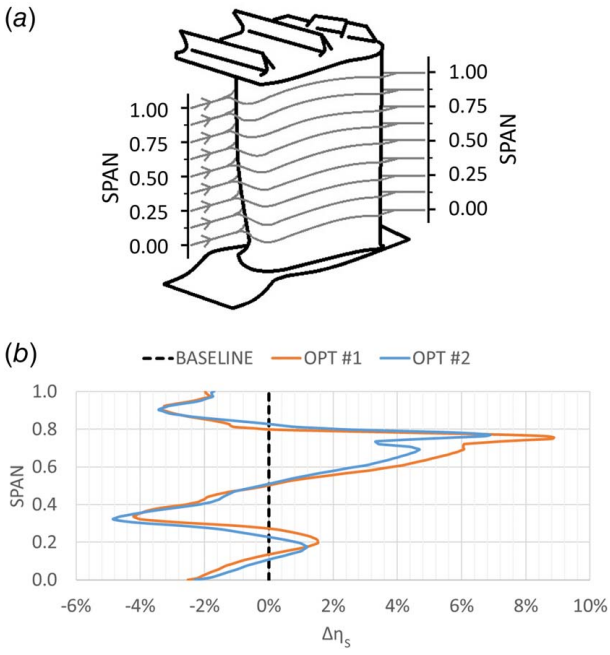

Fig. 10 Spanwise isentropic efficiency calculation for the baseline and optimal designs. Schematic of the "constant-span streamlines" used to perform the calculation (*a*). The plot in (*b*) shows the resulting streamline HPR isentropic efficiency deltas between each optimum and the baseline $\Delta\eta S = \eta S,OPT,i - \eta S,BSL$.

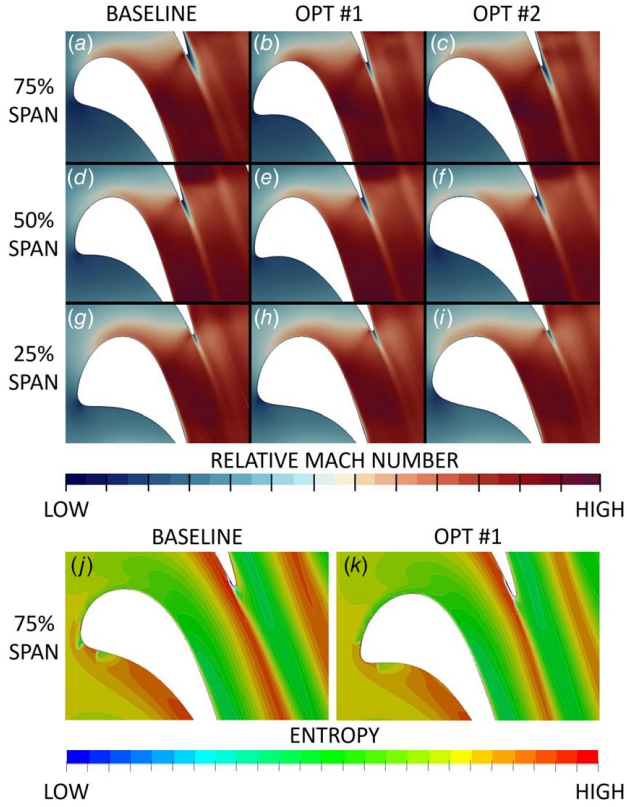

Fig. 11 Flow-field visualization with relative Mach number contours for all of the designs (*a*)–(*i*) and entropy contours for the baseline and OPT#1 (*j*) and (*k*) at constant-span sections. Pictures distorted.

some of the variations in aerodynamic efficiency pertaining to the different designs. In terms of aerodynamic efficiency, the designs generally appear to be highly sensitive to modifications in the trailing edge shape, and relatively insensitive to modifications in the leading edge shape. This is due to the large leading edge radius, and is in line with previous findings by the authors [4]. In Fig. 11, differences in relative Mach number can be seen at 75% span (i.e., Figs. 11(*a*)–11(*c*)), which is also where trailing edge elongation is taking place in the optimal designs (see Fig. 9(*b*)). This is the span height where both optimal designs outperform the baseline, as indicated in Fig. 10(*b*). In particular, both optimal designs managed to reduce the amount of flow separation in the trailing edge suction side area at 75% span when compared to the baseline. The positive effects of trailing edge elongation on wake losses are also displayed in the entropy contours (Figs. 11(*j*) and 11(*k*)), where the baseline design is compared with OPT #1 at 75% span. This deformation promotes a local reduction in throat area and an acceleration of the suction side flow with respect to the baseline case. At 50% span (Figs. 11(*d*)–11(*f*)), OPT#1's profile is remarkably similar to the baseline one. On the contrary, OPT#2 has a marked leading edge re-cambering toward the suction side, but this does not appear to have significant effects on either relative Mach contours or efficiency. At a 25% span, the effects of a trailing edge chord contraction can be seen in terms of a slight increase in throat area and lower peak velocities in the suction side area.

In summary, the optimizer ended up converging toward a high-span trailing edge extension for all the feasible optimal designs, which had to be counteracted by a trailing edge retraction in the lower half of the span to compensate for throat area and therefore comply with the capacity and reaction constraints. This effect can be seen in the spanwise efficiency plot of Fig. 10, where it is evident that the optimizer ended up trading off some efficiency at low span for a more substantial gain at high span. On the other

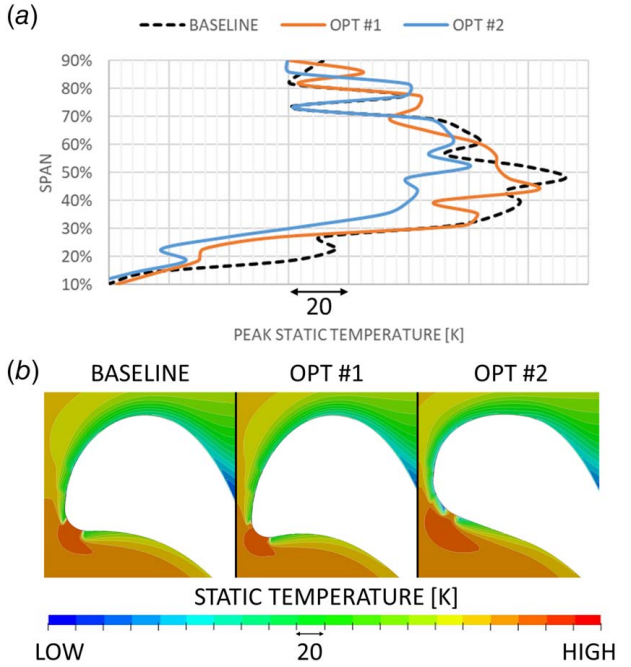

Fig. 12 Spanwise distribution of peak adiabatic recovery temperatures on the HPR surface for the baseline and optimal designs (*a*) and static temperature contours at a 50% span section with a close-up on the LE area for the baseline and optimal designs (*b*). Pictures in (*b*) are distorted.

hand, with OPT #2 (best-performing design for the thermal discipline), the optimizer adopted drastically different LE re-cambering choices. The motivation behind these choices becomes immediately evident after looking at the temperature plot of Fig. 12(*a*) and contours of Fig. 12(*b*). As mentioned in Sec. 4.1, the peak HPR adiabatic recovery temperatures for the conditions presently simulated are reached at about midspan near the flow stagnation point. In the plot of Fig. 12(*a*), the significant temperature reduction that made OPT #2 the best-performing design under the thermal aspect is clearly highlighted at 50% span. By looking at the temperature contours shown in Fig. 12(*b*) at midspan, it becomes clear that the significant LE re-cambering of OPT #2, combined with the film cooling strip positioning, had a beneficial effect on peak temperatures. Specifically, it resulted in a cooling row being moved in the way of the high-temperature gas stream that can be seen impinging on the LE in the other two cases (baseline and OPT #1).

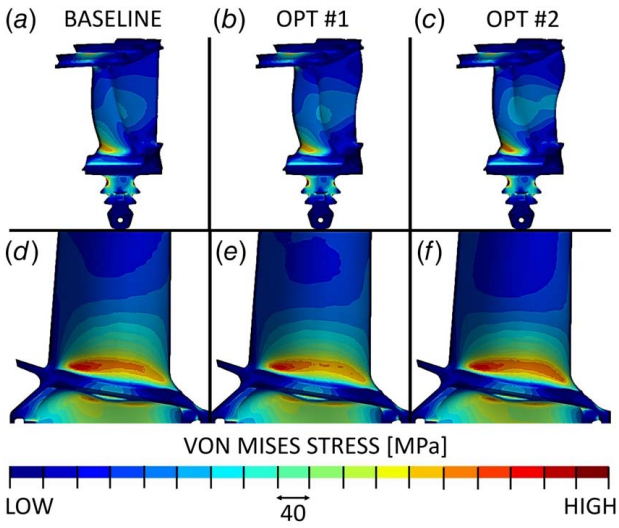

Fig. 13 Von Mises stress contours on the different designs—frontal views (*a*)–(c) and lateral views showing the suction side hub fillet area on the three cases (*d*)–(*f*). Pictures distorted.

Figure 13 shows contour plots of von Mises stress on the blade surface. Figures 13(*a*)–13(*c*) show frontal views for the baseline, first, and second optimum, respectively, while Figs. 13(*d*)–13(*f*) show close-up views of the suction side hub fillet area. The stress contours display a number of features, including contact stress at the firtree and root bending moment at the hub, which are commonly found in similar works by other authors, for example, in Refs. [47] and [48] with very similar patterns. A specific additional feature of this design is represented by a high-stress patch in the suction side fillet below the shroud, which is similar to what was found in Ref. [49] for a simplified shrouded design.

In the present work, the suction side hub fillet is the region of interest for stress, as discussed in the FEM methodology Sec. 2.4. In structural terms, as indicated by the triangular plot of Fig. 9(*a*), OPT #1 is the best-performing design, while OPT#2 only achieves a marginal (3 MPa) reduction. These reductions are achieved in the suction side hub fillet area, as shown in the contour plots of Figs. 13(*d*)–13(*f*) for the different designs. Both structures are slightly heavier than the baseline, with a +0.23% mass increase for OPT #1 and +0.14% for OPT #2. These values are measured by computing the volume of each structural mesh. In the case of OPT #1, stress reduction is achieved mainly by the high-span LE re-cambering visible in the section stacking of Fig. 9(*b*). The same pattern was observed by the authors on many low-stress design points from the Pareto front of Fig. 8. As a result of this re-cambering, a mass of metal is displaced toward the pressure side of the blade in the top half of the structure. This translates into a closer alignment of the blade sections' centers of mass with the radial direction, which lowers the bending moment experienced by the blade at the suction side hub fillet area. In the case of OPT #2, even if the peak stress value itself is lower than the baseline one, the entire suction side fillet is experiencing higher stresses on average, as displayed by the contours of Fig. 13(*f*).

4.3 High-Fidelity (Phase-Lag) Verification. The verification only deals with the thermal discipline, where the modeling of stator-rotor interaction was found to have the most significant impact. Previous studies published by the authors on the same baseline design indicated that, for proper prediction of the thermal quantities of interest on the HPR row, the unsteady stator–rotor interaction needs to be modeled.

In Ref. [33], it was found, on the baseline configuration, that steady-state calculated peak recovery temperatures were

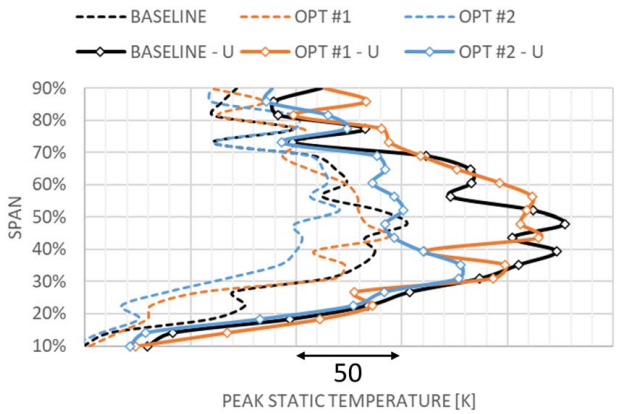

Fig. 14 Spanwise distribution of peak adiabatic recovery temperatures on the HPR surface for the baseline and optimal designs. Comparison between steady-state prediction (dashed) and unsteady prediction (solid, -U suffix for "Unsteady").

underestimated by approximately 100 K with respect to the more accurate phase-lag prediction. A similar prediction disagreement of approximately 120 K was found on a high-pressure turbine case study in Ref. [34]. Figure 14 shows a plot where the steady-state-predicted curves of Fig. 12(*a*) are compared with their phase-lag cycle-averaged counterparts. As expected, when stator-rotor interaction is modeled, peak HPR recovery temperatures increase by a significant amount (up to 75 K). Phase-lag predicts the same ranking for the different designs under the thermal aspect, i.e., OPT #2 is still the best-performing one, followed by OPT #1 and then the baseline. It is also interesting to note that the peak temperature margin between OPT #2 and the baseline has increased from 27.5 K of the steady-state prediction to 47.5 K of the phase-lag one. A phase-lag simulation is 30 times more costly than its steady-state counterpart, hence why the bulk of the optimization process was carried out in steady-state conditions.

4.4 Aerothermal Sensitivity Analysis. The objective of this part of the work is to assess the robustness of the baseline and optimal designs to realistic deterioration patterns. The data used for this analysis comes from a large measurement campaign conducted on in-service blades of the same model of the current baseline rotor. More details on this data and on the reverse-engineering methodology can be found in Ref. [4]. These deterioration data are applied, as described in Sec. 3.2, to the baseline and optimal designs obtained in the present study. It is worth stressing that these perturbations have been reverse-engineered on a set of in-service blades and thus are representative of real degradation patterns that are likely to repeat on any new design as well. Two robustness evaluations are conducted, first to assess the sensitivity to shroud deterioration and secondly to airfoil deformations. Figure 15 shows the effects of introducing increasingly high levels of shroud deterioration on the designs under study, in terms of high-pressure stage isentropic efficiency loss (Fig. 15(*a*)) and peak HPR recovery temperatures (Fig. 15(*b*)). The expected sharp drop in aerodynamic performance resulting from shroud deterioration is fundamentally unaffected by the change in design. In terms of peak HPR temperature, it can be seen in the graph of Fig. 15(*b*) that, for the baseline and OPT #1 design, there is a tendency of this quantity to decrease as a result of shroud deterioration. The opposite tendency is observed for OPT #2, which remains the thermally best-performing design even in the worst deterioration case.

Figure 16 displays, for the designs under study, the aerothermal performance variability, resulting from the propagation of the blade perturbations described in Fig. 7. On the vertical axes of Fig. 16, the plots show the frequency of each value within intervals of 0.005% for efficiency and 0.5 K for maximum temperature. The vertical arrows below the plots' horizontal axes represent the unperturbed objective function values. Figure 16(*a*) shows the effects of said perturbation on high-pressure stage isentropic efficiency, whereas Fig. 16(*b*) shows the effects of the same perturbations on peak HPR recovery temperatures. The baseline displays the best level of robustness for efficiency. Observing the perturbation's effect on efficiency (Fig. 16(*a*)), it can be seen that some of the perturbed designs outperform the respective unperturbed counterparts. All of the perturbed designs are found to be significantly non-compliant with the capacity and reaction constraints.

Both the baseline and OPT #1 designs show advantageous thermal reactions to the perturbations, as shown in Fig. 16(*b*), each distribution shifting to lower values when compared to the respective unperturbed conditions. On the contrary, OPT #2's thermal performance is the most sensitive to the perturbations, and all its perturbed variants achieve higher temperatures. This pattern seems to replicate what was seen for the effect of shroud deterioration on peak HPR temperatures (see Fig. 15(*b*)). This is due to the effect of perturbations (see Fig. 7), which are strongly biased in the positive direction. These perturbations result in re-cambering of the LE toward the suction side, which moves the film cooling strips upstream toward the stagnation point. In terms of thermal robustness, this mechanism, which allowed OPT #2 to gain its good thermal performance, shown in Fig. 12(*b*), is intrinsically unreliable. Further re-cambering of the LE leads to a drastic repositioning of the LE cooling hole rows. This once again allows the hot streak, which was originally impinging on the LE, to regain direct contact with the blade surface, causing a temperature rise, which happens in all the OPT#2 perturbed cases. On the

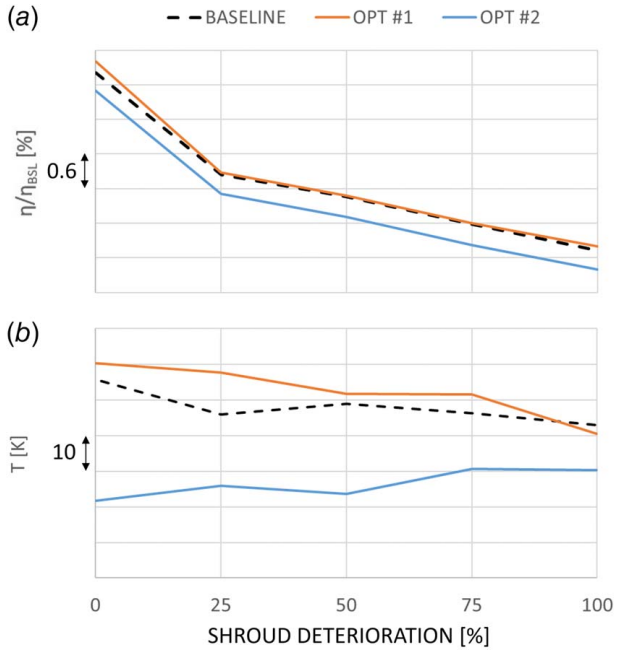

Fig. 15 Effects of the shroud deterioration levels displayed in Fig. 6(*a*) on efficiency nondimensionalized with respect to the baseline value (*a*) and peak HPR temperatures (*b*) on the designs under study.

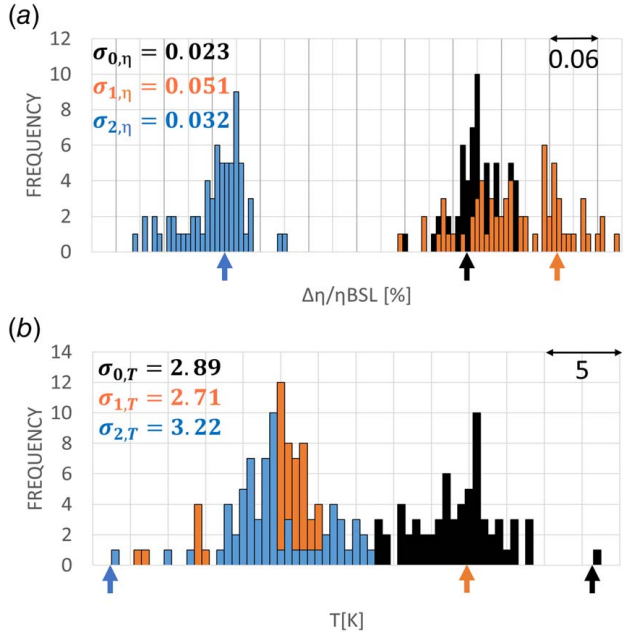

Fig. 16 Frequency distributions of efficiency non-dimensionalized with respect to the baseline value (*a*) and peak HPR temperatures (*b*) after propagation of the noise space depicted in Fig. 7 on airfoil design parameters, for the designs under study: Baseline (black), OPT#1 (orange), and OPT#2 (blue). Vertical arrows indicate the unperturbed values. Standard deviations are also displayed.

contrary, the baseline and OPT#1 designs, which start with zero or negative midspan LEMO, thermally benefit from this film cooling repositioning mechanism, brought on by the positive LEMO perturbation. As visible in Fig. 16(*b*), once the perturbation is introduced, OPT#2 ends up losing all its original thermal benefits with respect to OPT#1, forming mostly overlapping temperature distributions.

5 Conclusions

This article presents the results of a metamodel-based aerothermal-structural optimization of a modern film-cooled high-pressure turbine rotor. Few studies of this kind can be found in the literature due to the complexity of the problem, particularly when dealing with industrial geometries such as the one treated in the present work. The study shows that, when multi-disciplinarity is introduced and strict constraints are applied, the margins for improvement of modern existing designs become indeed quite narrow. However, relevant improvements can still be achieved, especially on the thermal side, which is extremely important for any high-pressure turbine rotor design in general.

The objective functions considered for this study are isentropic efficiency, peak rotor surface temperature, and peak rotor von Mises stress, respectively. The Rolls-Royce parametric design and rapid meshing system PADRAM are used to parametrize and mesh the geometries using a compact and orthogonal design space. The optimization is carried out by running CFD and FEM simulations, using Rolls-Royce industrial-grade solvers, to build an initial DoE. The open-source optimization suite GEMSEO is provided with the DoE data to train the metamodels and perform a constrained genetic optimization producing three-dimensional Pareto fronts.

Two feasible optimal designs are selected, achieving a peak stress reduction of 17.5 Mpa in conjunction with an efficiency increase of 0.16% (OPT #1) and a peak temperature reduction of 27.5 K (OPT #2). The thermal behavior of the designs is verified with unsteady simulations, confirming the steady-state findings. Finally, deterioration features reverse-engineered from a set of in-service blade scans are applied on the baseline and optimal designs, to assess their performance's robustness to real-life deterioration patterns.

The efficiency gain of OPT #1 is found to be mainly related to a TE re-cambering and extension, taking place in the top half of the span, which grants better flow attachment and lower wake dissipation, in conjunction with LE re-cambering at the midspan section. The outstanding thermal performance of OPT #2 is due to the combination of a LE re-cambering interacting with one of the LE film cooling strips. Film cooling plays a vital role and must be parametrized to properly empower the optimizer. This is applicable to any film-cooled design that is being optimized under the thermal aspect. The stress reduction achieved by OPT#1 was found to be due to a more radial stacking of the airfoil sections, brought in by the LE re-cambering.

The relevance of modeling the stator-rotor interaction, at least as a final verification step of the optimal designs' thermal performance, is highlighted. This is true in general for any high-pressure turbine, where hot streak migration takes place and must be properly modeled, as steady-state results are found to be consistently "colder" than their unsteady counterparts.

Robustness assessment reveals that OPT #2's thermal performance is the most sensitive to in-service deterioration taking place below the shroud, and all designs appear to be equally affected by shroud deterioration. Robustness must be assessed using real engine data. As was the case for the present work, real deformations are often biased, which can more easily be destabilizing for some designs' performance.

Acknowledgment

The authors would like to thank Rolls-Royce plc for their support and permission to publish this work. This work has been conducted within the framework of the NEXTAIR project. The NEXTAIR project has received funding from the European Union's Horizon Europe research and innovation program under grant agreement No 101056732.

Conflict of Interest

There are no conflicts of interest.

Data Availability Statement

Data provided by a third party listed in Acknowledgements.

Nomenclature

H	=	enthalpy, J kg^{-1}
T	=	HPR adiabatic recovery temperature, K
BSL	=	baseline rotor blade design
CSD	=	casing cooling downstream to the rotor blade
CSF	=	casing cooling upstream to the rotor blade
DELT	=	blade section circumferential lean adjustment
DoE	=	design of Experiments
DSH	=	hub cavity inflow downstream to the rotor blade
HPR	=	high-pressure rotor
HPS	=	high-pressure stator
HPT	=	high-pressure turbine
HTEC	=	HPS TE cooling slot
IPS	=	intermediate-pressure stator
ITEC	=	IPS TE cooling slot
LE, TE	=	leading edge, trailing edge
LEMO/TEMO	=	blade section LE/TE re-cambering
OPT #i	=	optimum rotor blade design number *i*
PS, SS	=	pressure side, suction side
RANS	=	Reynolds-averaged Navier–Stokes
RBF	=	radial basis function
SKEW	=	blade section stagger angle variation
SVM	=	Von Mises stress, MPa
USH	=	hub cavity inflow upstream to the rotor blade
η	=	HPT stage isentropic efficiency
η_S	=	streamline isentropic efficiency

References

[1] Glezer, B., 2004, *VKI LS 2004-02, Turbine Blade Tip Design and Tip Clearance Treatment*, von Karman Institute for Fluid Dynamics, Rhode-St-Genese, Belgium, pp. 1–23.
[2] Rolls-Royce plc, 2015, *The Jet Engine*, 5th ed., Wiley, New York, United Kingdom.
[3] Ruffles, P. C., 1991, *Trenchard Lecture*, Cambridge University Press, Cambridge, UK.
[4] Carta, M., Ghisu, T., and Shahpar, S., 2022, "High-Fidelity CFD Analysis of In-Serviced Shrouded High-Pressure Turbine Rotor Blades," ASME J. Turbomach., **144**(12), p. 121001.
[5] Virdis, I., Ghisu, T., Shahpar, S., De La Puerta, I., and Li, H., 2022, "Digital Shadow and Robust Optimization of In Service Squealer Tip Turbine Blades," ASME Turbo Expo, Rotterdam, The Netherlands, June 14–16.
[6] Carta, M., Ghisu, T., and Shahpar, S., 2023, "Heat Transfer Analysis of Damaged Shrouded High-Pressure Turbine Rotor Blades," Int. J. Turbomach. Propul. Power, **8**(3), p. 24.
[7] Rolls-Royce plc. "Trent-1000," https://www.rolls-royce.com/~/media/Files/R/Rolls-Royce/documents/civil-aerospace-downloads/28071 7-Trent-1000-infographic.pdf, Accessed September 10, 2024.
[8] Shahpar, S., 2011, "Challenges to Overcome for Routine Usage of Automatic Optimisation in the Propulsion Industry," Aeronaut. J. New Ser., **115**(1172), pp. 615–625.
[9] Shahpar, S., 2004, "A Review of Automatic Optimisation Applications in Aerodynamic Design of Turbomachinery Blades," Design Optimization International Conference, Athens, Greece, Mar. 31–Apr. 2.
[10] Toropov, V. V., Filatov, A. A., and Polynkin, A. A., 1993, "Multipatameter Structural Optimization Using FEM and Multipoint Explicit Approximations," Struct. Optim., **6**(1), pp. 7–14.
[11] Cuciumita, C., John, A., Qin, N., and Shahpar, S., 2021, "Structurally Constrained Aerodynamic Adjoint Optimisation of Highly Loaded Compressor Blades—GT2021-59717," Asme Turbo Expo 2021, Virtual, June 7–11.
[12] Shahpar, S., Toropov, V. V., and Polynkin, A. A., 2008, "Large Scale Optimization of Transonic Axial Compressor Rotor Blades—AIAA

2008-2056," AIAA/ASME/ASCE/AHS/AHC Structures, Structural Dynamics and Materials Conference, Schaumburg, IL, Apr. 7–10.
[13] Shahpar, S., and Lapworth, L., 2003, "PADRAM: Parametric Design and Rapid Meshing System for Turbomachinery Optimisation, GT2003-38698," ASME Turbo Expo and International Joint Power Generation Conference, Atlanta, GA, June 16–19, pp. 579–590.
[14] Seshadri, P., Shahpar, S., and Parks, G. T., 2014, "Robust Compressor Blades for Desensitizing Operational Tip Clearance Variations—GT2014-26624," ASME Turbo Expo 2014, Dusseldorf, Germany, June 16–20.
[15] Sasaki, D., and Obayashi, S., 2005, "Efficient Search Trade-Offs by Adaptive Range Multi Objective Genetic Algorithms," J. Aerospace Comput. Inf. Commun., **2**(1), pp. 44–64.
[16] Hu, K., Ju, Y., Feng, Y., and Zhang, C., 2022, "A Dimension Reduction-Based Multidisciplinary Design Optimization Method for High Pressure Turbine Blades," ASME J. Turbomach., **144**(9), p. 091011.
[17] Song, Y., Guo, Z., Song, L., LI, J., and Feng, Z., 2014, "Multi-Objective and Multi-Disciplinary Optimization of Gas Turbine Blade Profile and Cooling System Using Conjugate Heat Transfer Analysis," ASME Turbo Expo 2014, Dusseldorf, Germany.
[18] Amaral, S., Verstraete, T., Van den Braembussche, R., and Arts, T., 2010, "Design and Optimization of the Internal Cooling Channels of a High Pressure Turbine Blade—Part I: Methodology," ASME J. Turbomach., **132**(2), p. 021013.
[19] Verstraete, T., Amaral, S., Van dem Braembussche, R., and Arts, T., 2010, "Design and Optimization of the Internal Cooling Channels of a High-Pressure Turbine Blade—Part II: Optimization," ASME J. Turbomach., **132**(2), p. 021014.
[20] Martins, J., and Ning, A., 2021, *Engineering Design Optimization*, Cambridge University Press, ISBN 9781108833417, Cambridge.
[21] Gallard, F., Vanaret, C., Guénot, D., Gachelin, V., Lafage, R., Pauwels, B., Barjhoux, P. J., and Gazaix, A., 2018, "GEMS: A Python Library for Automation of Multidisciplinary Design Optimization Process Generation," 2018 AIAA/ASCE/AHS/ASC Structures, Structural Dynamics, and Materials Conference, Kissimmee, FL, Jan. 8–12.
[22] Erdos, J. L., and Alzner, E., 1977, "Computation of Unsteady Transonic Flows Through Rotating and Stationary Cascades," NASA CR-2900.
[23] He, L., 1990, "An Euler Solution for Unsteady Flows Around Oscillating Blades," ASME J. Turbomach., **112**(4), pp. 714–722.
[24] He, L., 2010, "Fourier Methods for Turbomachinery Applications," Prog. Aerosp. Sci., **46**(8), pp. 329–341.
[25] Salvadori, S., Adami, P., and Martelli, F., 2011, "On the Implementation of a Phase Lag Approach for Multi-Row Simulations," Proceedings of the 10th International Symposium on Experimental, Computational Aerothermodynamics of Internal Flows, Brussels, Belgium, July 4–7.
[26] Schnell, R., 2004, "Investigation of the Tonal Acoustic Field of a Transonic Fan Stage by Time-Domain CFD Calculations with Arbitrary Blade Counts, ASME Paper GT2004-54216," Turbo Expo: Power for Land, Sea, and Air, Vienna, Austria, June 14–17.
[27] Gerolymos, G. A., Michon, G., and Neubauer, J., 2002, "Analysis and Application of Chronochronic Periodicity in Turbomachinery Rotor/Stator Interaction Computations," J. Propul. Power, **18**(6), pp. 1139–1152.
[28] Crawford, M., Kays, W., and Moffat, R., 1980, "Full-coverage film cooling on flat, isothermal surfaces: Data and predictions," NASA Contractor Report (CR) 3219—Stanford University, Stanford, California, January 1, 1980.
[29] Demargne, A. A. J., Evans, R. O., Tiller, P. J., and Dawes, W. N., 2014, "Practical and Reliable Mesh Generation for Complex, Real World Geometries," AIAA 52nd Aerospace Sciences Meeting, National Harbor, MD, Jan. 13–17.
[30] Lapworth, L., 2004, "Hydra CFD: a Framework for Collaborative CFD Development," International Conference on Scientific and Engineering Computation (IC-SEC), Singapore, June 30–July 2.
[31] Chilla, M., Hodson, H., and Newman, D., 2013, "Unsteady Interaction Between Annulus and Turbine Rim Seal Flows," ASME J. Turbomach., **135**(5), p. 051024.
[32] Menter, F. R., 1994, "Two-Equation Eddy-Viscosity Turbulence Models for Engineering Applications," AIAA J., **32**(8), pp. 1598–1605.
[33] Carta, M., Shahpar, S., and Ghisu, T., 2024, "Analysis of the Aerothermal Performance of Modern Commercial High-Pressure Turbine Rotors Using Different Levels of Fidelity," Proc. Inst. Mech. Eng., Part A: J. Power Energy (8), pp. 1426–1442.
[34] Carta, M., Shahpar, S., Ghisu, T., and Licheri, F., 2024, "Multi-Fidelity Modelling of the Effect of Combustor Traverse on High-Pressure Turbine Temperatures," Aerospace, **11**(9), p. 750.
[35] Salvadori, S., Martelli, F., and Adami, P., 2010, "Development of Phase Lag Approach for the Numerical Evaluation of Unsteady Flows, ICFD10-EG-3702," International Congress of Fluid Dynamics, Ayn Soukhna, Egypt, Dec. 16–19.
[36] Armstrong, I., and Edmunds, T., 1989, "Fully Automatic Analysis in the Industrial Environment," Proceedings of the Second International Conference of Quality Assurance in Finite Element Analysis, NAFEMS, Stratford-upon-Avon, England.
[37] Pohl, J., Thompson, H. M., Valencia, A. G., López Juste, G., Fico, V., and Clayton, G. A., 2017, "Structural Deflection's Impact in Turbine Stator Well Heat Transfer," ASME J. Eng. Gas Turbines Power, **139**(4), p. 041901.
[38] Sobol, I. M., 1967, "On the Distribution of Points in a Cube and the Approximate Evaluation of Integrals," USSR Comput. Math. Math. Phys., **7**(4), pp. 86–112.
[39] Shahpar, S., 2014, *VKI* Lecture Series, Von Karman Institute for Fluid Dynamics, Sint-Genesius-Rode, Belgium.
[40] Carta, M., Ghisu, T., and Shahpar, S., 2023, "Multi-Fidelity Heat Transfer Analysis of Shrouded High-Pressure Turbine Rotor Blades," ASME Turbo Expo 2023, Boston, MA, June 26–30.
[41] Carta, M., Ghisu, T., and Shahpar, S., 2024, "Combustor Traverse Optimization to Lower High-Pressure Turbine Rotor Temperatures," ASME Turbo Expo 2024, London, UK, June 24–28.
[42] Ainley, D. G., and Mathieson, G. C. R., 1951, *A Method of Performance Estimation for Axial-Flow Turbines*, Vol. 2974, British Aeronautical Research Council R&M, 31, p. 1.
[43] Baljé, O. E., and Binsley, R. L., 1968, "Axial Turbine Performance Evaluation. Part A—Loss-Geometry Relationships," J. Eng. Power, **90**(4), pp. 341–348.
[44] Mukhtarov, M. K., and Krichakin, V. I., 1969, "A Procedure for Estimating Losses in the Flow Path of Axial Turbines in Calculating Their Characteristics," Teploenergetika, **7**, pp. 26–31.
[45] Denton, J. D., 1993, "Loss Mechanisms in Turbomachines," ASME J. Turbomach., **115**(4), pp. 621–656.
[46] Kerrebrock, J., and Mikolajczak, A., 1970, "Intra-Stator Transport of Rotor Wakes and Its Effect on Compressor Performance," ASME J. Eng. Power, **92**(4), pp. 359–368.
[47] Durelli, A. J., Dally, J. W., and Mey, W. F., 1958, "Stress and Strength Studies on Turbine Blade Attachments," Proc. Soc. Exp. Stress Anal., **10**(6), pp. 171–186.
[48] Van Nimwegen, R. R., and Tepper, S. "High Pressure Turbine Blade Stress Analysis," Nasa Technical Report, Torrance, California, 1972.
[49] Boyle, R. J., Agricola, L. M., Parikh, A. M., Ameri, A. A., and Nagpal, V. K., 2018, "Shrouded CMC Rotor Blades for High Pressure Turbine Applications, GT2018-76827," ASME Turbo Expo, Oslo, Norway, June 11–15.